Experimental Validation of a Phased Array Probe Model in Ultrasonic Inspection

Ultrasonics 108 (2020) 106217

Contents lists available at ScienceDirect

Ultrasonics

journal homepage: www.elsevier.com/locate/ultras

Experimental validation of a phased array probe model in ultrasonic inspection

Xiangyu Lei[a,*], Håkan Wirdelius[a], Anders Rosell[b]

[a] Department of Industrial and Materials Science (IMS), Chalmers University of Technology, SE-412 96 Gothenburg, Sweden
[b] GKN Aerospace Sweden AB, Flygmotorvägen 1, SE-461 81 Trollhättan, Sweden

ARTICLE INFO

Keywords:
Experiment
Modeling
Phased array
Validation

ABSTRACT

New manufacturing technologies such as additive manufacturing facilitate flexible and complex designs and production of components. However, these new techniques should not compromise the safety aspect, which imposes higher demands on the integrity insurance and inspection methods. Phased array ultrasonic testing (PAUT) provides advanced inspection and evaluation processes, whereas qualification is still needed when applied together with new manufacturing techniques. Numerical modeling, as one of the potential qualification methods, has been developed for decades and should be validated before practical applications. This paper presents an experimental validation work of the phased array probe model implemented in a software, simSUNDT, by comparing the maximum echo amplitudes between the physical experiments and simulations. Two test specimens with side-drilled holes (SDHs) and different materials are considered for validation and practical purposes. An experimental platform with a mechanized gantry system, which enables stabilized inspection procedure, is built and applied during the validation work. Good correlations can be seen from the comparisons and this model is concluded as an acceptable alternative to the corresponding experimental work. The relation between depth and beam angle is also noticed and investigated, which is essential to guarantee an accurate inspection.

1. Introduction

New manufacturing technologies such as additive manufacturing (AM) have emerged in industries to enable new design concepts and to facilitate production of complex components. The application of these new technologies should however not compromise safety, a critical aspect in most industries. This leads to higher demands on the methods to ensure the integrity of the components. Nondestructive evaluation (NDE) as a collection of methods, enables inspection without interfering with the integrity and functionality of the manufactured components, is widely used among industries. Ultrasonic testing (UT) as one of the NDE methods, plays an important role in the inspection process, especially with the use of phased array (PA) techniques, which enable enhanced signal processing and specific optimizations for the cases that previously were not possible to achieve with conventional single element UT. The advantages of the PA techniques over the conventional single element UT are revealed in terms of, e.g. fast, flexible beam steering and focusing ability with a single PA probe, application of imaging algorithms and optimized delay law specific for an inspection situation. However, new techniques and corresponding evaluation procedures should be comprehensively qualified before practical applications. Future practical applications may especially be challenged by AM where part integrity needs to be assured on a net shaped geometry with inherent process variability. The traditional qualification methods involve extensive and expensive experiments on test pieces, which means that many variables need to be characterized and limited to situations relevant for the specific application. The cost of creating representative test pieces can be significant. Specific challenges can be to manufacture representative defects in critical locations or in large numbers for statistical evaluations such as probability of detection (POD) assessments. However, such experimental work can be assisted or even partly be replaced by mathematical models developed in recent decades, with the aim to facilitate simulations of the inspection procedure. Examples of these are the Thompson-Gray Measurement Model used in UTSim [1], the Elastodynamic Finite Integration Technique (EFIT) [2], the Finite Element Method (FEM) model used in terms of TOFD technique [3] and CIVA [4]. These models provide the possibility to simulate the whole process of UT inspection and generate results corresponding to the relevant experiments. Besides, the models can also be important for understanding the physical principles and system optimizations regarding

* Corresponding author.
E-mail addresses: xlei@chalmers.se (X. Lei), hakan.wirdelius@chalmers.se (H. Wirdelius), anders.ar.rosell@gknaerospace.com (A. Rosell).

https://doi.org/10.1016/j.ultras.2020.106217
Received 24 February 2020; Received in revised form 24 June 2020; Accepted 26 June 2020
Available online 03 July 2020

equipment and procedure design [5,6]. However, before applying these models, they need to be thoroughly validated by either comparing the simulation results with other already validated models, or with physical experiments. For example, Lopez et al. [7] investigated the possibility of applying PAUT on inspection of AM components, where CIVA was utilized to simulate the inspection process and was experimentally validated in the end. Avramidis et al. [8] used CIVA to design a proper PA probe for railway solid axles inspection by beam pattern simulation, and it was experimentally compared for validation. Chatillon et al. [9] validated the simulated FMC-TFM imaging capabilities in CIVA by experiments. It was shown that CIVA can produce good image and amplitude predictions. The simulation model implemented in the software, simSUNDT, developed by Chalmers University of Technology in Sweden, has been experimentally validated [10–13] by comparing the simulation results with the ultrasonic benchmark study [14]. This study was initiated by the World Federation of NDE Centres with experimental results provided by Commissariat a l'énergie atomique (CEA, France). The model renders satisfactory results in terms of conventional contact probes. The recently developed PA probe model implemented in the software had however, been validated only to a limited extent [15] using the benchmark study. In order to facilitate more comprehensive experiments and make full use of the experimental data for validation, an experimental platform was built at the Department of Industrial and Materials Science (IMS), Chalmers University of Technology. The platform consists of a mechanized gantry system for high accuracy transducer positioning and an ultrasonic testing data acquisition unit with PA configuration. In this paper the focus is to further validate the PA probe model in simSUNDT by experiments. A physical PA contact probe with wedge is used towards side-drilled holes (SDHs) as defects in noise-free aluminum and stainless-steel test specimens. The developed experimental platform is described and used for the model validation. A relation between the beam angle and the defect depth is then investigated and compared with the simulation.

2. simSUNDT software

The simSUNDT software consists of a Windows-based pre-processor in order to specify the parameters that define the simulation, and a postprocessor for analysis of the simulated result. The software exploits a mathematical kernel UTDefect [10–12,16], which does the actual mathematical modeling part. The UTDefect Fortran code has been developed at Chalmers University of Technology and it has previously been validated to some extent by comparing with available experimental data [10–13]. The 3D elastodynamic wave equation that defines the wave propagation in a homogeneous half space is solved by using vector wave functions [16]. The modeled geometry can also be limited by a totally reflecting backwall and thus be described as a plate with finite or infinite thickness bounded by the scanning surface, on which the scanning sequences are defined by rectangular mesh. The scattering by the individual defect is solved using analytical or semi-analytical methods. Volumetric defects are treated by separation-of-variables. Strip-like, circular, and rectangular cracks are treated by hypersingular integral equation methods.

The software can simulate the entire NDE inspection, i.e. the combination of used technique and procedure. Thus, the software includes a calibration option with reference reflectors. The side-drilled hole (SDH) is represented by a cylindrical cavity [17] and the flat-bottom hole (FBH) is approximated by an open circular crack.

The analytical approach, however, limits the morphological structure of the defects into well-defined mathematical volumes and surfaces, though having correct crack tip behaviour (i.e. diffraction). The volumetric defects include a spherical/spheroid cavity (pore), a spherical inclusion (isotropic material differing from the surrounding material, i.e. slag) and a cylindrical cavity (SDH). Crack-like defects include in the software at this stage is a rectangular/circular crack and a surface breaking strip-like crack. Tilting planar back surface could also be modeled for the strip-like crack, but otherwise it is assumed parallel to the scanning surface. The surface-breaking strip-like crack and the rectangular crack close to the back surface can be used to model the corresponding defects in the test piece (e.g. lack of fusion or fatigue crack).

The conventional contact probe is represented in the mathematical model as the boundary condition representing a plane wave in the far-field at a certain angle. This enables the simulation of most probes commercially available on the market, by specifying related parameters such as wave types, crystal size and shape, angles, frequency ranges and contact conditions. To model the receiver, a reciprocity argument [18] is applied. The arrangement of the probe can be pulse-echo, separate with fixed transmitter and tandem configuration (TOFD). These principles are the same for the PA probe model in which each individual element being represented by corresponding boundary conditions. The individual boundary conditions are translated into the main coordinate system and a phased array wave front with certain nominal angle is formulated by constructive phase interference. The PA model enables a focusing effect by deploying the delay law of individual element. The formulated nominal angle can also be altered by a specific delay law, but it should be noted that this is only possible for small angles without any wedge specified.

3. Experimental method

3.1. Experimental equipment

The data acquisition hardware unit TOPAZ64 from ZETEC company is a 64-channel phased array ultrasonic testing equipment. Ultrasonic data is communicated between TOPAZ64 and a computer physically by Gigabyte ethernet cable and is processed by corresponding software UltraVision on the computer.

The PA probe used in the experiments with notation of LM-5MHz from ZETEC is a 64-crystal linear phased array longitudinal-wave probe with nominal center frequency of 5 MHz and bandwidth of 74%. Each element has a size of 0.5 mm in the primary axis and 10 mm in the secondary axis (elevation). With the kerf of 0.1 mm, the total aperture of the probe is 38.3 mm in the primary axis and 10 mm in elevation, see Fig. 1 for the nomination convention of a general linear PA probe dimension. Table 1 lists all relevant technical specifications for the linear PA probe used in the experiments.

Two ZETEC probe-matched wedges, denoted as LM-0LW and LM-55SW shown in Fig. 2, were used for non-angled and angled inspection, respectively. Together with the angled wedge (LM-55SW), the probe is capable of generating 55-degree shear wave into carbon steel (wave speed = 3230 m/s) without specifying delay law for the elements. It is

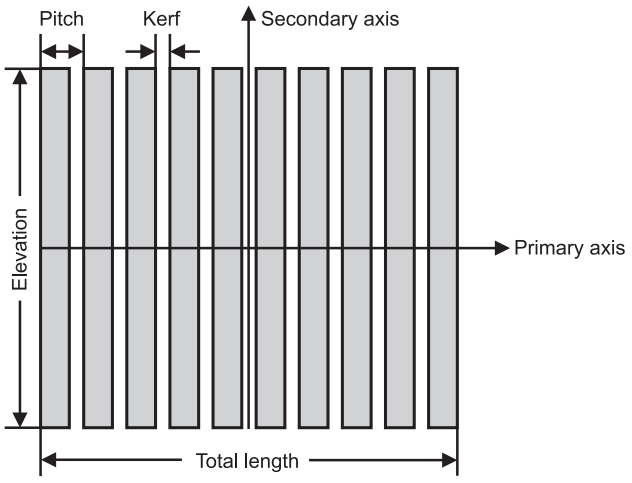

Fig. 1. Nomination convention of PA probe dimension.

Table 1
Specification of the linear PA probe used in the experiment.

Specification	Value
Total elements	64
Total length (mm)	38.3
Elevation (mm)	10
Pitch (mm)	0.6
Kerf (mm)	0.1
Connector type	ZPAC
Cable length (m)	2.5
Center frequency (MHz)	5
Relative bandwidth (%)	74

otherwise capable of providing 40 to 70-degree azimuthal scanning by certain delay laws.

3.2. Mechanized gantry system

To provide an accurate scanning procedure with high repeatability, a mechanized gantry system was developed and used. This experimental system enables different data presentation probabilities, such as B- and C-scan that require probe position (encoder) information. The probe position can thus be retrieved from the in-built encoders in the stepper motors and the generated B- and C-scan are available directly for data interpretation.

Fig. 3 shows the mechanized gantry system on the platform. It is a three-axes gantry system, while only two horizontal axes (X- and Y-axis) are motor-controlled at this stage. The corresponding encoder signal is transmitted to the TOPAZ64 to locate the probe position. The vertical position of Z-axis is manually adjusted by rotating the top guide screw. The Z-axis together with a fixture with spring load capability is used to apply a constant pressure of the probe onto the scanning surface of the specimen.

3.3. Test specimens

There were two test specimens used in the validation work. The artificial defects considered were SDHs, all with the same diameter of 3 mm, drilled into the specimens. One of the SDHs was taken as the reference defect in the corresponding test specimen. It should be noted that the FBH could also be drilled and treated as the reference defect, as an option in the simSUNDT software. However, as indicated in [15] the FBH might lead to variations in results due to the potentially non-planar bottom surface from the actual manufacturing.

The first test specimen is a 320*100*30 mm (length*height*width) flat surface aluminum block with longitudinal and transverse wave speed of 6320 m/s and 3130 m/s, respectively. The depth of the SDHs range from 20 mm from the scanning surface to 90 mm with an increment of 5 mm, ordered consecutively from one side to the other. The

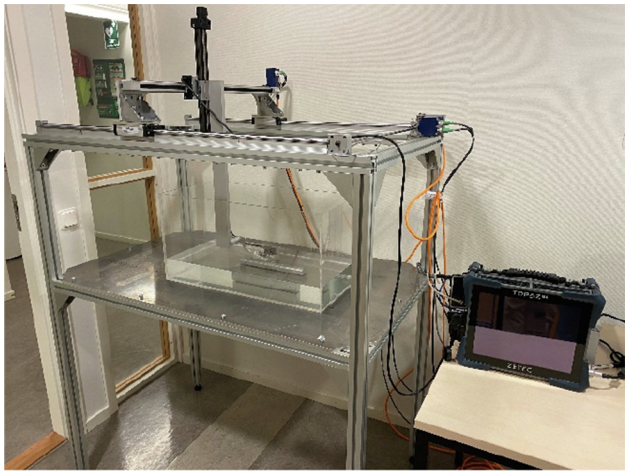

Fig. 3. Mechanized gantry system on the experimental platform.

second test specimen is a 140*130*30 mm (length*height*width) flat surface stainless-steel block with longitudinal and transverse wave speed of 5624 m/s and 3238 m/s, respectively. The depth of the SDHs range from 20 mm to 115 mm from four different scanning surfaces, with an increment of 5 mm but not ordered consecutively under the same surface. The four scanning surfaces considered are denoted by the letters A to D. The surface notation and detailed locations of the SDHs are presented in the sketches of the two test specimens shown in Figs. 4 and 5 for the aluminum and the stainless-steel specimen, respectively. All the dimensions are in unit of millimetres and note that the sketches only show the profile with the location of SDHs, i.e. in the length-height perspective of the specimens. The presented validation work focuses mainly on the aluminum specimen as it is suitable for probe validation due to its homogenous and isotropic material properties, as well as low absorption and scattering characteristics. In addition, it has a long scanning surface that facilitates mechanized inspection over many SDHs in one continuous scanning. The stainless-steel specimen is used afterwards as a complement in order to include the validation in a more realistic material type that is often encountered during UT inspection.

3.4. Experimental setup

The PA probe used in the experiments and simulations operates in pulse-echo mode. This is not a limitation, neither in the system nor the software. The experiments towards the SDHs in these test specimens aim at detecting the maximum direct echo responses under non-angled and 45-degree angled inspections with and without focusing effect. Only the central 16 elements were activated to avoid ghost images during the unfocused inspection, while all 64 elements were activated to generate proper focusing effect at certain depths of interest. In a

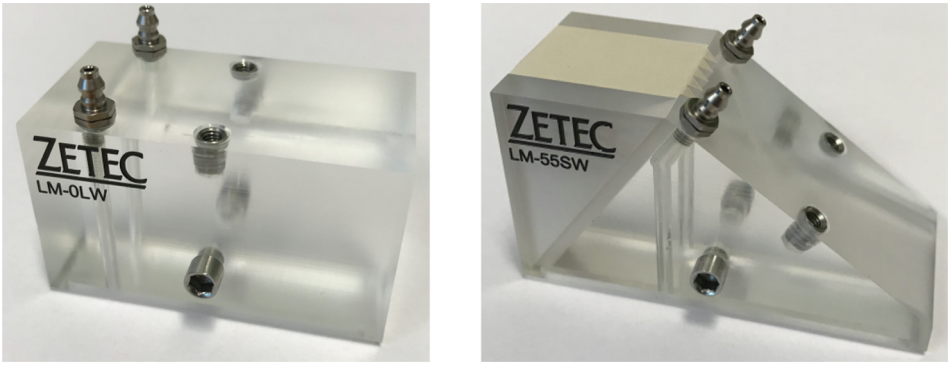

Fig. 2. Probe-matched ZETEC wedges, LM-0LW (left) and LM-55SW (right).

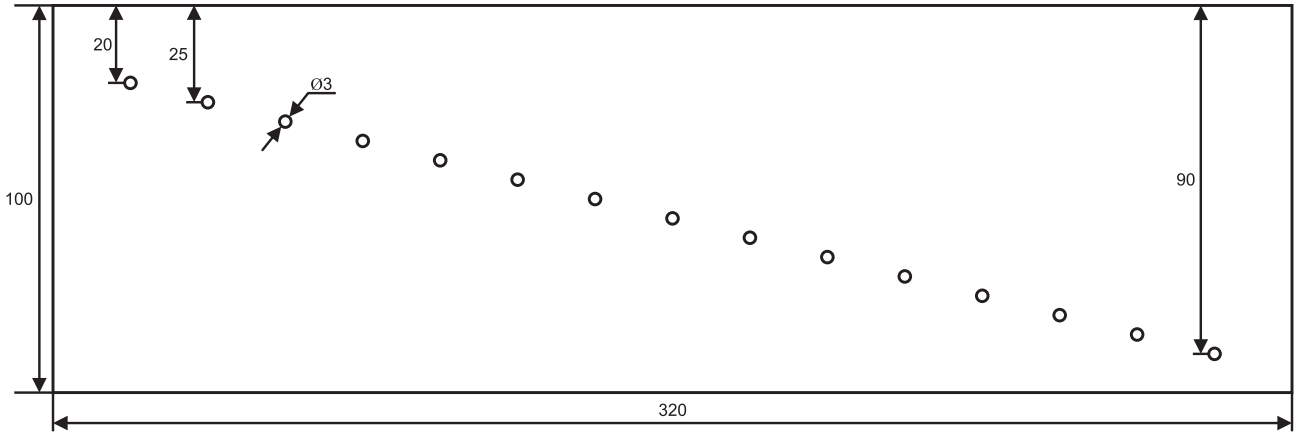

Fig. 4. Aluminum test specimen with 15 SDHs at different depth with diameters of 3 mm.

single run, the PA probe performed a continuous one-line scan over all SDHs on the scanning surface from one end to the other, in the same procedure settings as in the simulation. Then, the maximum echo amplitude of each SDH could be retrieved from the recorded data.

The inspections mainly focus on the aluminum test specimen (Fig. 4) thanks to its long scanning surface that ensures consistency in probe alignment for all positions using the mechanized gantry system. All the SDHs are physically reachable from the scanning surface for the non-angled inspection on this aluminum test specimen, while only 11 SDHs ranging from 20 mm to 70 mm with an increment of 5 mm can be reached for the 45-degree angled inspection due to the limited sample size. All echo amplitudes were normalized with respect to the reference SDH located at the focusing depth used during the inspection, they were otherwise normalized with SDH at 50 mm depth. Regarding the

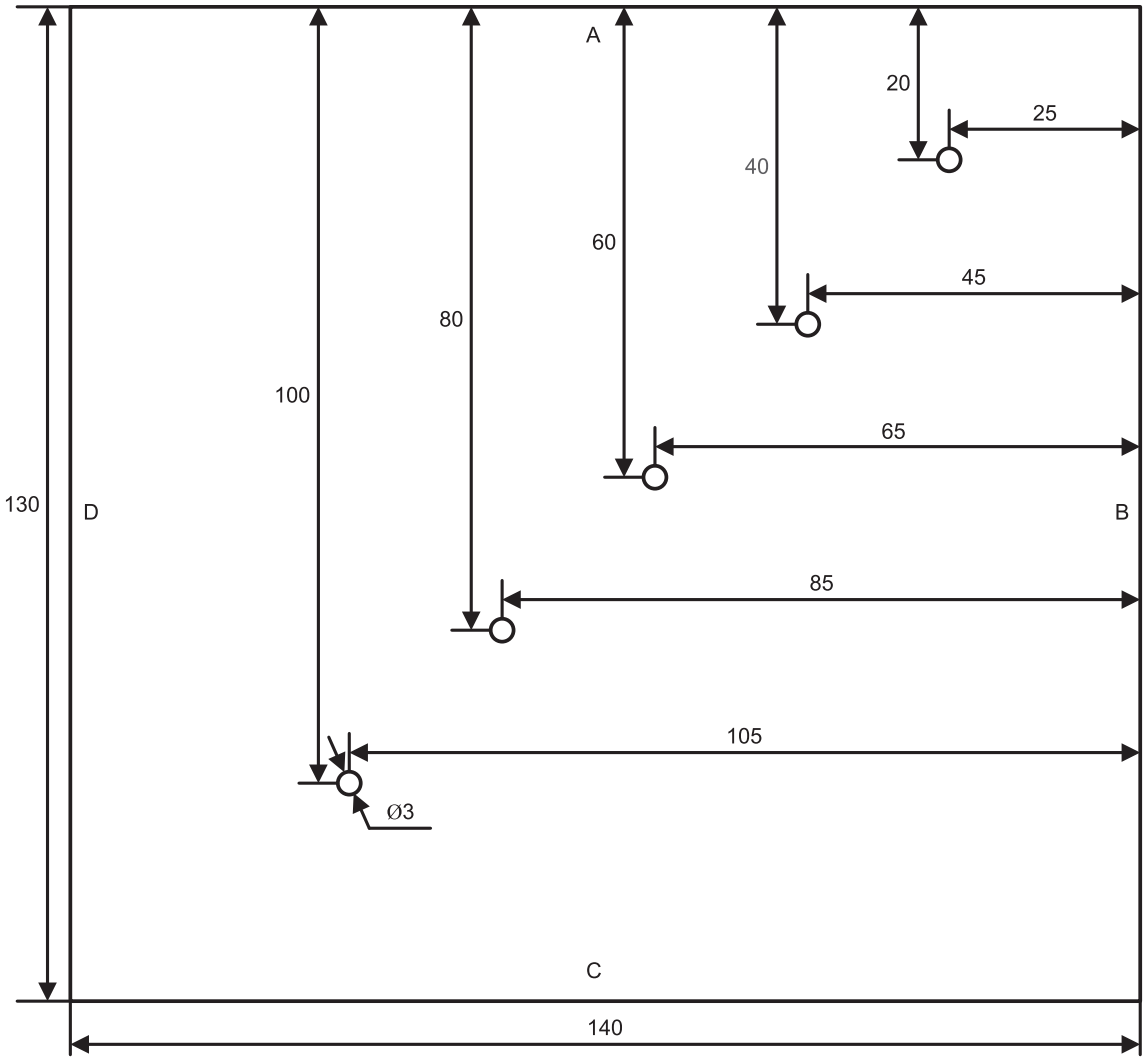

Fig. 5. Stainless-steel test specimen with 5 SDHs at different depth with diameters of 3 mm.

stainless-steel test specimen (Fig. 5), only the non-angled inspections without focusing effect were performed due to the limited scanning space for 45-degree angled inspection. Besides, the inspections were separated into 4 groups upon each scanning surface in accordance with its geometry. The reason for this was that the backwall depths are different to each scanning surface and it was inappropriate to normalize all signals towards the same reference signal, i.e. a specific backwall echo. Thus, the echo amplitudes were processed separately based on which scanning surface they belong to, and the echo amplitudes were normalized with respect to the middle SDH belonging to the corresponding scanning surface instead.

Each set of the experiments was repeated five times. For each repetition the probe was moved continuously in a one-line scan from the same starting point on the scanning surface. All other experimental conditions were unchanged between repetitions to ensure consistency. Experimental results are thus expressed by the average value and the variation in experimental values are gathered and represented by error bars in the result presentations. The echo amplitudes for all SDHs were recorded in percentage of screen height with the same gain values for consistency. Amplitude normalization towards the reference SDH was performed using:

$$dB = 20\log_{10}\left(\frac{A_{SDH}}{A_{Ref}}\right) \quad (1)$$

where A_{SDH} is the echo amplitude of the SDH of interest and A_{Ref} is the counterpart of the reference SDH. Normalized results in decibel (dB) were used in comparisons. It was observed during the experiments that a strong echo occurs at a certain depth in the A-scan due to the wave reflection within the non-angled wedge used. This strong echo can mask the echo reflected from an actual SDH at a similar depth. For this reason, the SDH at 85 mm depth in the aluminum specimen and 75 mm depth in the stainless-steel specimen is undetectable and is thus excluded from the analysis.

4. Results and discussion

The experiments were performed mainly on the aluminum specimen with the same parameters used in the corresponding simulations. Echo amplitudes were then normalized based on the same reference SDH so that the results are comparable under the same scale.

4.1. Non-angled inspection

The results for the non-angled inspection on the aluminum specimen are presented without focusing effect in Fig. 6 and with focusing depth at 50 mm, 70 mm and 90 mm in Figs. 7, 8, 9, respectively. In each figure, the upper part presents the normalized echo amplitudes for SDHs and the lower part shows the corresponding differences between the experimental and simulated results in terms of absolute value. Note again that the amplitude normalizations were performed using the SDH at 50 mm depth in the non-focusing case and at the individual focusing depth in the focusing cases.

The non-angled inspection without focusing effect (Fig. 6) indicates good agreement between the experiments (asterisk signs) and the simulations (circle signs). The differences (solid-circle line) for most SDHs are within 1 dB for SDHs down to 75 mm in depth. The discrepancy for SDHs deeper than 75 mm could be due to attenuation in the experiments. Attenuation in this case could be material damping (grain scattering and viscous damping) and/or deviation in beam divergence due to boundary conditions that was not included in the current simulations.

When the focusing depth of 50 mm is set for the non-angled inspection (Fig. 7), the simulations (circle signs) show the same amplitude trend as in the experiments (asterisk signs), i.e. more energy is reflected from the SDHs positioned close to the focusing depth. The

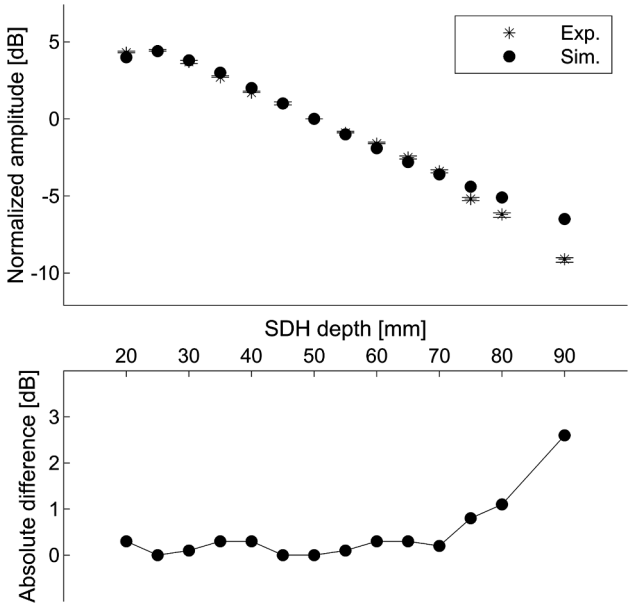

Fig. 6. Results comparison on aluminum specimen for the non-angled inspection without focusing effect.

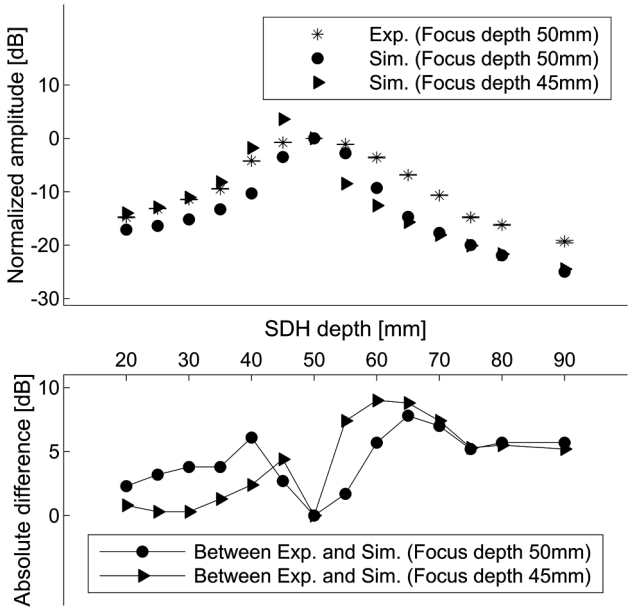

Fig. 7. Results comparison on aluminum specimen for the non-angled inspection with focusing depth at 50 mm.

discrepancies in the range of interest from 45 to 55 mm depth are within 3 dB (solid-circle line). To show the flexibility of the simulation model and the effect of a shallower focusing depth, a series of simulations with focusing depth of 45 mm are included (right-pointing triangle signs). It is indicated in Fig. 7 that a 5 mm decrease of focusing depth in this case retains the focusing trend, while the echo amplitudes in the range of interest differ much comparing to the experiments (solid-triangle line).

When the focusing depth is set at 70 mm for the non-angled inspection (Fig. 8), the comparisons show similar correspondence as in the 50 mm focusing case. The discrepancies within the focusing range of interest, i.e. between 65 mm and 75 mm depth, are around 1 dB (solid-circle line). But it should be noticed in the experimental results (asterisk signs) that the maximum echo amplitude does not occur at 70 mm depth, where the focusing depth is set, but at around 65 mm

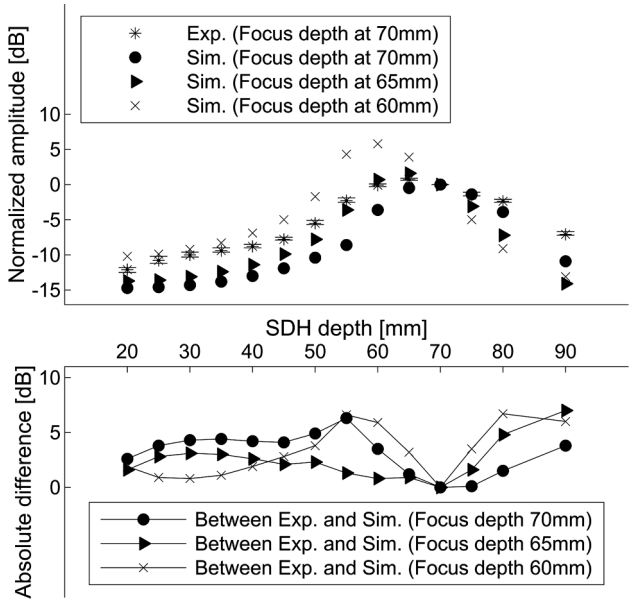

Fig. 8. Results comparison on aluminum specimen for the non-angled inspection with focusing depth at 70 mm.

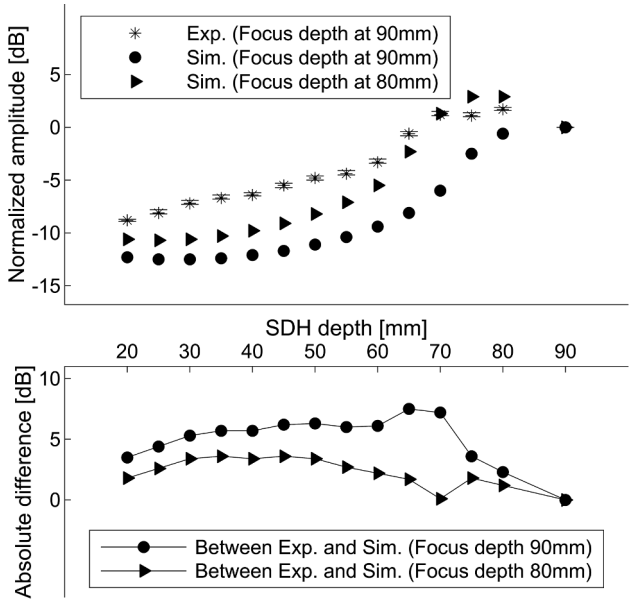

Fig. 9. Results comparison on aluminum specimen for the non-angled inspection with focusing depth at 90 mm.

depth instead. This phenomenon indicates that the actual focusing depth in the experiment could be less than the specified depth at 70 mm, as Azar indicated in their beam simulation findings [19]. Thus, another two series of simulations with focusing depth at 60 mm (cross signs) and 65 mm (right-pointing triangle signs) were carried out and compared with the experiments. A better correspondence can be observed when the simulated focusing depth is set at 65 mm (solid-triangle line), even outside the focusing region of interest.

When the focusing depth is set at 90 mm for the non-angled inspection (Fig. 9), the same phenomenon can be noticed in the experiments as previous results, i.e. the maximum echo amplitude is not from the SDH at 90 mm depth, but from a shallower SDH at around 80 mm. Regarding the simulation, it is important to see that the simulations with focusing at 90 mm depth (circle signs), i.e. the same focusing depth set in the experiments, differ much comparing with the experiments (asterisk signs). This could be caused by an increasing mismatch between the specified and the actual focusing depth when the focusing depth gets deeper, found by Sun [20] during numerical simulation of the sound beam. Thus, a series of simulations with focusing depth at 80 mm were conducted (right-pointing triangle signs), which lead to a better agreement between the experiments and the simulations (solid-triangle line) within the focusing depth range. The differences are then at most 2 dB in this case in the focusing range of interest.

When it comes to the stainless-steel test specimen, the SDHs that can be reached from the same scanning surface are grouped and processed to create a dataset for each surface, since there is no specific backwall echo that can be considered as the general reference signal for normalization. This also reduces the irrelevant variations for the current study caused by small changes of probe alignment between each surface. Explicitly, the SDHs were grouped based on their scanning surfaces nominated by the letters A to D, see Fig. 5. To ensure the accuracy of normalization, the echo amplitudes were normalized towards the middle SDH in each group. It again should be noted that for the group belonging to surface B, the SDH in the middle (at depth of 75 mm) was undetectable due to the masking effect of the strong echo from the non-angled wedge. Thus, the echo amplitudes in this group were instead normalized by the SDH at 55 mm depth. The corresponding results comparisons are presented in Fig. 10. Clear correlations are seen in each group and the overall difference is within 2 dB.

4.2. 45-degree angled inspection

Regarding the angled inspection on aluminium specimen with nominal refracted angle of 45 degree, the inspections were performed without focusing effect (Fig. 11) and with focusing effect at depths of 50 mm (Fig. 12) and 70 mm (Fig. 13). Similarly, the upper part of each figure presents the normalized echo amplitudes for SDHs and the lower part shows the corresponding differences between the experimental and simulated results in terms of absolute value. The mismatch is at most 2 dB for non-focusing case shown in Fig. 11 (solid-circle line), which gives a good correlation. When the focusing depth at 50 mm is considered, good correlations with at most 2 dB mismatch can be seen in Fig. 12 (solid-circle line) within the focusing depth range of interest from 45 mm to 55 mm. Similar correlations for focusing depth of 70 mm are presented in Fig. 13 (solid-circle line) within the focusing depth range of interest around 70 mm.

Furthermore, it is worth noticing in Figs. 7, 8, 9, 12 and 13 that when the beam focusing effect is involved, the deviations between the experimental and simulated results are large outside the focusing depth range of interest. Since 64 probe elements were used in the focusing cases, the calculated near field length is around 270 mm beneath the probe surface, which potentially contributes to the deviations by the wave intensity fluctuations and uncertainties. Attenuation in the experiments, e.g. material damping (grain scattering and viscous damping) or contact conditions that was not included in the current simulations could also be a potential aspect to the deviation. Thus, the model should be used with care if the target defect is not located around the focusing depth.

4.3. Depth-angle relation

Taking a closer look at the experimental results in case of angled inspections, it can be noticed that the true beam angle where the maximum echo amplitude is obtained can be different with respect to defect depth. The calculation of this true beam angle is based on Fig. 14, in which p is the half path length of wave propagation when the echo amplitude reaches maximum. D is the SDH depth seen from the scanning surface to the center axis of the SDH and r is the radius of this SDH. The true beam angle θ can thus be calculated as:

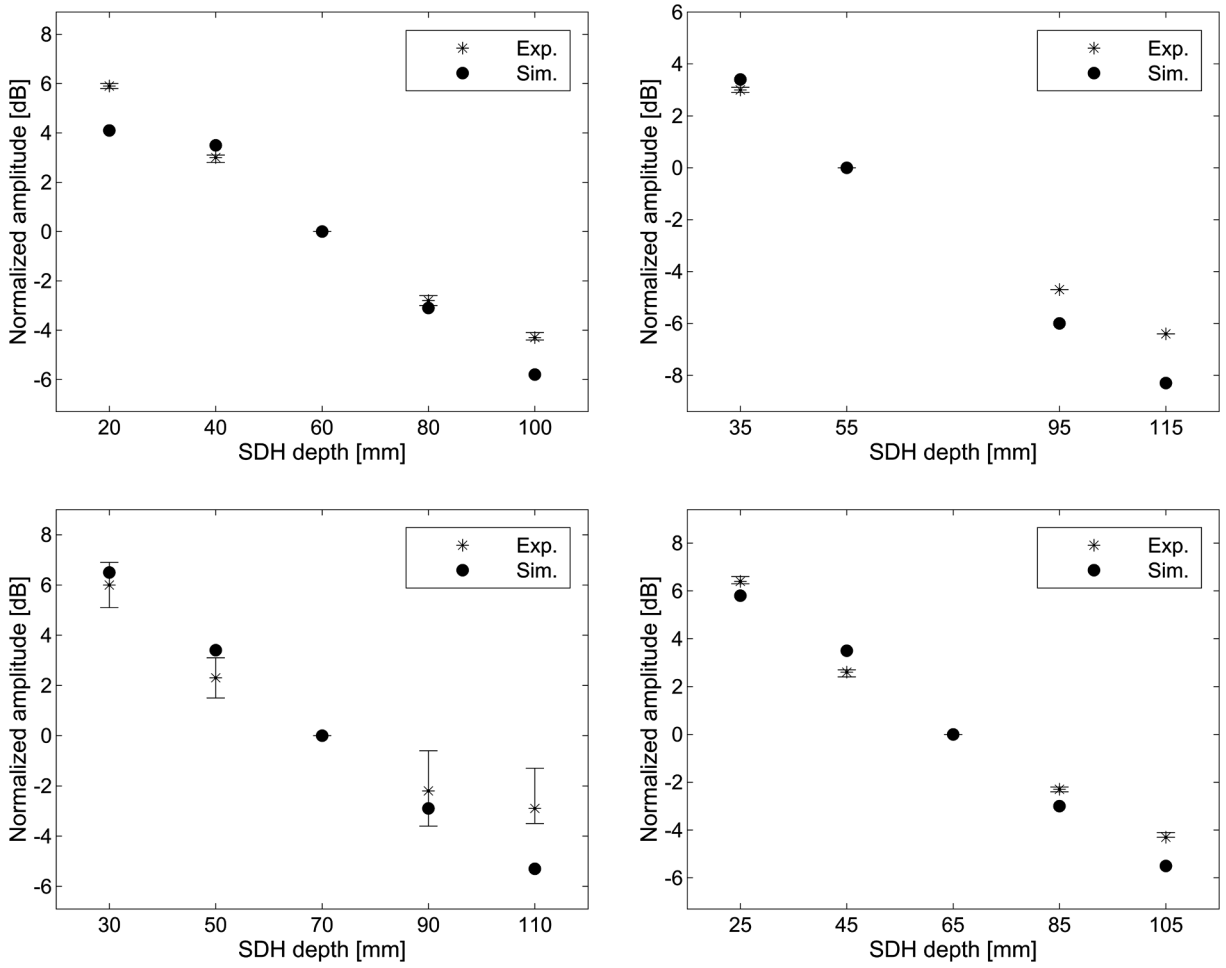

Fig. 10. Results comparison on stainless-steel specimen for the non-angled inspection without focusing effect a) on surface A normalized by SDH at 60 mm depth; b) on surface B normalized by SDH at 55 mm depth; c) on surface C normalized by SDH at 70 mm depth; d) on surface D normalized by SDH at 65 mm depth.

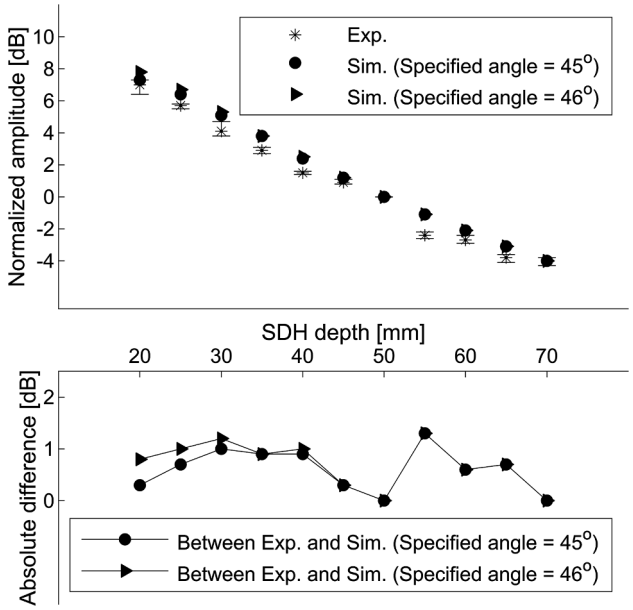

Fig. 11. Results comparison on aluminum specimen for the angled inspection without focusing effect.

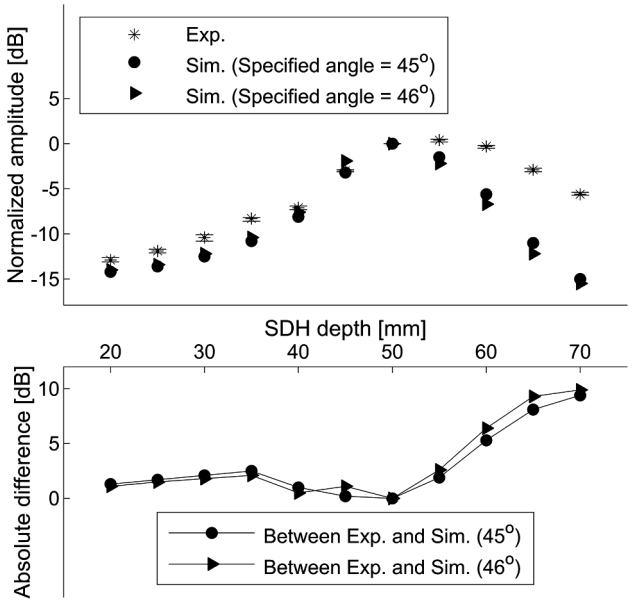

Fig. 12. Results comparison on aluminum specimen for the angled inspection with focusing depth at 50 mm.

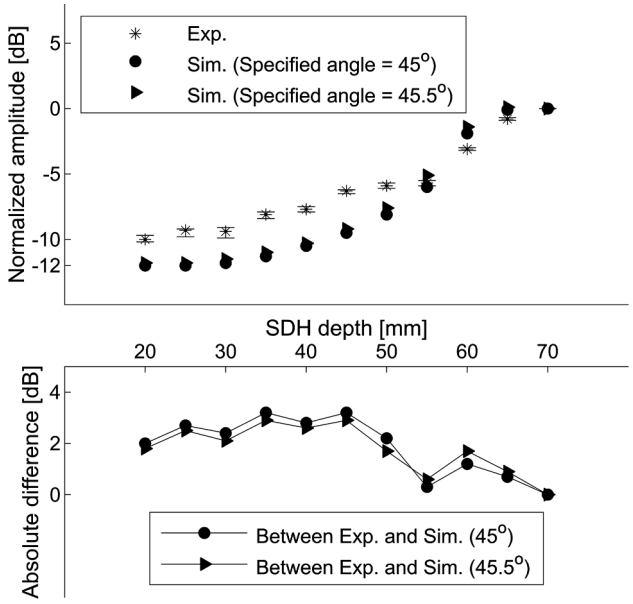

Fig. 13. Results comparison on aluminum specimen for the angled inspection with focusing depth at 70 mm.

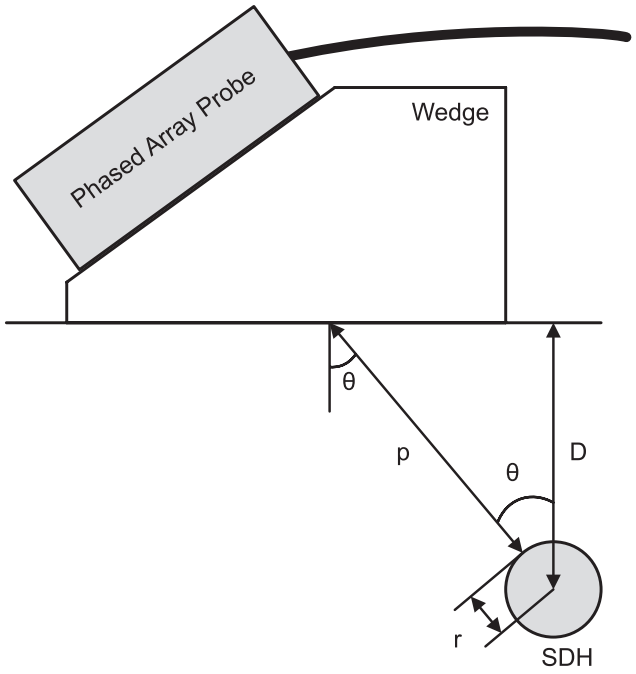

Fig. 14. Parameters for the determination of depth-angle relation.

$$\theta = \cos^{-1}\left(\frac{D}{p+r}\right) \quad (2)$$

The half path length of wave propagation for each SDH can be retrieved from the A-scan in the experiments and simulations. The aluminum test specimen (r = 3 mm) was used in this investigation, where the nominal refracted angle used was 45 degrees.

When the focusing depth is at 50 mm, the depth-angle relation can be seen in Table 2. It is obvious that the calculated true angle θ of the main beam at each depth is different in both the simulations and in the experiments. Specifically, the true beam angle obtained at the focusing depth of 50 mm in the experiments reaches 46 degrees while the counterpart from the simulations is still around 45 degrees.

To ensure the accuracy of the simulation results, especially within the focusing depth range of interest, i.e. from 45 mm to 55 mm depth in this case, a new set of simulations with prescribed nominal refracted angle of 46 degrees were conducted and the true beam angle is then presented in Table 3. The angle of 45.96 degrees at 50 mm depth correlates better with the experiments under this configuration, and the corresponding echo amplitudes for SDHs are plotted in Fig. 12 (right-pointing triangle sign) to verify the influence by the change of nominal refracted angle. It can be noticed that the echo amplitudes are slightly influenced, and the discrepancies increase to at most 3 dB within the focusing depth range of interest (solid-triangle line).

Regarding the inspection with a focusing depth at 70 mm, a true angle of the main beam is calculated as 45.5 degrees at the focusing depth following the same procedure as for the previous case, thus a series of simulations with a prescribed nominal refracted angle of 45.5 degrees were performed, which end up with a similar true beam angle of 45.6 degrees at 70 mm depth. The corresponding echo amplitudes are shown in Fig. 13 (right-pointing triangle sign) and the mismatch rises to at most 2 dB instead within the focusing depth range at around 70 mm (solid-triangle line).

Table 2
Depth-angle relation when focusing depth of 50 mm and nominal refracted angle of 45-degree is used in the simulation.

	Simulations			Experiments		
D (mm)	p (mm)	p + r (mm)	θ (°)	p (mm)	p + r (mm)	θ (°)
20	21.73	23.23	30.58	22.21	23.71	32.49
25	31.00	32.50	39.72	30.56	32.06	38.76
30	38.65	40.15	41.65	39.16	40.66	42.45
35	46.83	48.33	43.60	47.47	48.97	44.38
40	54.78	56.28	44.71	55.32	56.82	45.25
45	62.40	63.90	45.23	63.40	64.90	46.10
50	69.29	70.79	45.06	70.46	71.96	45.99
55	76.05	77.55	44.83	77.34	78.84	45.76
60	83.00	84.50	44.76	84.23	85.73	45.58
65	89.85	91.35	44.64	91.10	92.60	45.42
70	98.29	99.79	45.45	97.98	99.48	45.28

Table 3
Depth-angle relation when focusing depth of 50 mm and nominal refracted angle of 46-degree is used in the simulation.

	Simulations			Experiments		
D (mm)	p (mm)	p + r (mm)	θ (°)	p (mm)	p + r (mm)	θ (°)
20	22.39	23.89	33.16	22.21	23.71	32.49
25	30.97	32.47	39.65	30.56	32.06	38.76
30	39.48	40.98	42.94	39.16	40.66	42.45
35	47.89	49.39	44.88	47.47	48.97	44.38
40	55.92	57.42	45.84	55.32	56.82	45.25
45	63.54	65.04	46.22	63.40	64.90	46.10
50	70.43	71.93	45.96	70.46	71.96	45.99
55	77.45	78.95	45.84	77.34	78.84	45.76
60	84.42	85.92	45.71	84.23	85.73	45.58
65	91.41	92.91	45.60	91.10	92.60	45.42
70	100.15	101.65	46.48	97.98	99.48	45.28

5. Conclusion

This paper presents a mechanized operation platform aiming for ultrasonic inspection and the experimental validation work performed using this platform towards a developed PA probe model. A correlation between the depth of defect and the corresponding true beam angle was briefly investigated. Two different test specimens with side-drilled holes at different depths and materials were manufactured and involved in this work. Since the validation of the transmitter/receiver model was only addressed, the aluminum piece was mainly used in the current

work. Non-angled and angled inspections with and without focusing effect were compared with their corresponding simulations to show the accuracy of the simulation model, and the accompanying parametric studies showed the flexibility of the model. It can be concluded from these comparisons that the PA probe model implemented in this simulation software, simSUNDT, can provide acceptable UT results, in terms of maximum echo amplitudes. The model can thus be treated as an alternative to the physical experimental work to some extent. The phenomenon of shallower actual focusing depth than the nominal one found by the sound field simulation was also observed experimentally, thus leading to a confirmed variation and discrepancy of the focusing depth in the reality. The relation between the defect depth and the corresponding true angle of the main beam emphasizes the necessity of calibration towards a calibration specimen that is similar to the actual block to be inspected regarding material properties, potential defect depth, etc. It again reveals the possibility of the flexible parametric study of the simulation model. However, one should still be aware of the limitation that the defects considered in this study are only SDHs since they are easy to manufacture with well-defined properties and more importantly, can provide direct and clear echoes to be compared with. In terms of the inspection with focusing effect, larger mismatches between experiments and simulations are observed on the defects lying outside the focusing depth of interest. These mismatches might come from the near field effect and sound wave attenuation. Attenuation includes beam divergence and material damping, whereas the latter is currently not considered in the simulations because of the low absorption assumption to the aluminum test specimen, and of the validation focus on the PA probe model rather than on material aspects. While the material damping is an option in the simSUNDT and shall be further explored in the future work. Nevertheless, it should still be noted that the focusing depth needs to be carefully specified with respect to the certain defect of interest for accurate simulation purpose.

CRediT authorship contribution statement

Xiangyu Lei: Methodology, Validation, Investigation, Data curation, Writing - original draft, Visualization. **Håkan Wirdelius:** Conceptualization, Resources, Writing - review & editing, Supervision, Funding acquisition. **Anders Rosell:** Writing - review & editing, Visualization, Funding acquisition.

Declaration of Competing Interest

The authors declare that they have no known competing financial interests or personal relationships that could have appeared to influence the work reported in this paper.

Acknowledgments

This work was carried out within a collaboration project between GKN Aerospace Engine Systems and Chalmers University of Technology, Sweden. The funding from the Swedish innovation agency VINNOVA (reference number 2017-04856) within the national aeronautical research program (NFFP7) is greatly acknowledged. The technical assistance by Farham Farhangi and Daniel Snögren from the Swedish Qualification Centre (SQC) is highly appreciated. I would also like to thank my supervisor Håkan Wirdelius and Anders Rosell for the supervision of my research work, and my parents and my close friend Hao Wang for their encouragements to my research studies.

References

[1] M. Garton, T. Gray, R.B. Thompson, I. Gray, D.O. Thompson, D.E. Chimenti, UTSIM: overview and application, in: AIP Conf. Proc., 2010: pp. 2141–2148. https://doi.org/10.1063/1.3362394.
[2] P. Fellinger, R. Marklein, K.J. Langenberg, S. Klaholz, Numerical modeling of elastic wave propagation and scattering with EFIT — elastodynamic finite integration technique, Wave Motion. 21 (1995) 47–66, https://doi.org/10.1016/0165-2125(94)00040-C.
[3] Z. Tang, M. Yuan, H. Wu, J. Zhang, H.-J. Kim, S.-J. Song, S.-S. Kang, FEM Model-Based Investigation of Ultrasonic TOFD for Notch Inspection, J. Korean Soc. Nondestruct. Test. 34 (2014) 1–9, https://doi.org/10.7779/JKSNT.2014.34.1.1.
[4] P. Calmon, Recent developments in NDT simulation, in: WCU, 2003: pp. 443–446.
[5] R.B. Thompson, Simulation models: critical tools in NDT engineering, Mater. Eval. 63 (2005) 300–308.
[6] E.R. Generazio, C.E. Harris, The role of modelling and simulation in the development of advanced non-destructive evaluation systems, Aeronaut. J. 103 (1999) 325–328, https://doi.org/10.1017/S0001924000064691.
[7] A.B. Lopez, J. Santos, J.P. Sousa, T.G. Santos, L. Quintino, Phased Array Ultrasonic Inspection of Metal Additive Manufacturing Parts, J. Nondestruct. Eval. 38 (2019) 62, https://doi.org/10.1007/s10921-019-0600-y.
[8] S. Avramidis, D. Yan, D. Liaptsis, S. Michau, A. Ngyendinh, Ultrasonic modelling to design a phased array probe for the testing of railway solid axles from the end face, in: 52nd Annu. Conf. Br. Inst. Non-Destructive Test. 2013, NDT 2013, British Institute of Non-Destructive Testing, 2013: pp. 500–511.
[9] S. Chatillon, S. Robert, P. Brédif, P. Calmon, G. Daniel, F. Cartier, Results of the 2014 UT modeling benchmark obtained with models implemented in CIVA: Solution of the FMC-TFM ultrasonic benchmark problem using CIVA, in: 2015: pp. 1847–1855. https://doi.org/10.1063/1.4914810.
[10] P.A. Jansson, Modeling of ultrasonic detection of a rectangular crack, in: AIP Conf. Proc., AIP, 2000: pp. 57–64. https://doi.org/10.1063/1.1306034.
[11] A. Bostrom, A.S. Eriksson, Scattering by two penny-shaped cracks with spring boundary conditions, Proc. R. Soc. London. Ser. A Math. Phys. Sci. 443 (1993) 183–201. https://doi.org/10.1098/rspa.1993.0139.
[12] P. Bövik, A. Boström, A model of ultrasonic nondestructive testing for internal and subsurface cracks, J. Acoust. Soc. Am. 102 (1997) 2723–2733, https://doi.org/10.1121/1.420326.
[13] H. Wirdelius, Experimental validation of the UTDefect simulation software, in: Proc. 6th Int. Conf. NDE Relat. to Struct. Integr. Nucl. Press. Components, Budapest, 2007.
[14] Benchmark Problems, (n.d.). https://www.wfndec.org/benchmark-problems/ (accessed April 28, 2020).
[15] H. Wirdelius, The implementation and validation of a phased array probe model into the simSUNDT software, in: Proc. 11th Eur. Conf. NDT, 2014.
[16] A. Boström, H. Wirdelius, Ultrasonic probe modeling and nondestructive crack detection, J. Acoust. Soc. Am. 97 (1995) 2836–2848, https://doi.org/10.1121/1.411850.
[17] A. Boström, P. Bövik, Ultrasonic scattering by a side-drilled hole, Int. J. Solids Struct. 40 (2003) 3493–3505, https://doi.org/10.1016/S0020-7683(03)00150-1.
[18] B.A. Auld, General electromechanical reciprocity relations applied to the calculation of elastic wave scattering coefficients, Wave Motion. 1 (1979) 3–10, https://doi.org/10.1016/0165-2125(79)90020-9.
[19] L. Azar, Y. Shi, S.-C. Wooh, Beam focusing behavior of linear phased arrays, NDT E Int. 33 (2000) 189–198, https://doi.org/10.1016/S0963-8695(99)00043-2.
[20] F. Sun, Z.M. Zeng, S.J. Jin, S.L. Chen, Sound-field of discrete point sources simulation on deflecting and focusing of near-field of ultrasonic phased array, J. Syst. Simul. 25 (2013) 1108–1112. https://doi.org/10.16182/j.cnki.joss.2013.05.006.